A&A 643, L12 (2020)
https://doi.org/10.1051/0004-6361/202039458

Astronomy & Astrophysics

LETTER TO THE EDITOR

Parsec-scale properties of the radio brightest jetted AGN at $z > 6$

C. Spingola[1,2], D. Dallacasa[1,2], S. Belladitta[3,4], A. Caccianiga[3], M. Giroletti[2], A. Moretti[3], and M. Orienti[2]

[1] Dipartimento di Fisica e Astronomia, Università degli Studi di Bologna, Via Gobetti 93/2, 40129 Bologna, Italy
[2] INAF – Istituto di Radioastronomia, Via Gobetti 101, 40129 Bologna, Italy
e-mail: spingola@ira.inaf.it
[3] INAF – Osservatorio Astronomico di Brera, Via Brera, 28, 20121 Milano, Italy
[4] DiSAT, Università degli Studi dell'Insubria, Via Valleggio 11, 22100 Como, Italy

Received 17 September 2020 / Accepted 20 October 2020

ABSTRACT

We present Director's Discretionary Time multi-frequency observations obtained with the *Jansky* Very Large Array and the Very Long Baseline Array (VLBA) of the blazar PSO J030947.49+271757.31 (hereafter PSO J0309+27) at $z = 6.10 \pm 0.03$. The milliarcsecond angular resolution of our VLBA observations at 1.5, 5, and 8.4 GHz unveils a bright one-sided jet extended for ∼500 parsecs in projection. This high-z radio-loud active galactic nucleus is resolved into multiple compact sub-components that are embedded in a more diffuse and faint radio emission that enshrouds them in a continuous jet structure. We directly derive limits on some physical parameters from observable quantities such as viewing angle and Lorentz and Doppler factors. If PSO J0309+27 is a genuine blazar, as suggested by its X-ray properties, then we find that its bulk Lorentz factor must be relatively low (lower than 5). This value would be in favour of a scenario currently proposed to reconcile the paucity of high-z blazars with current predictions. Nevertheless, we cannot exclude that PSO J0309+27 is seen under a larger viewing angle, which would imply that the X-ray emission must be enhanced, for example, by inverse Compton scattering with the cosmic microwave background. More stringent constraints on the bulk Lorentz factor in PSO J0309+27 and on these factors in the other high-z blazars are necessary to test whether their properties are intrinsically different from those of the low-z blazar population.

Key words. galaxies: active – galaxies: jets – early Universe – techniques: high angular resolution – techniques: interferometric – quasars: individual: PSO J030947.49+271757.3

1. Introduction

Little is known observationally above redshift $z = 6$, at time when the Universe was young and the first sources (including active galactic nuclei, AGNs) ionised their surrounding gas in the period called cosmic reionisation (e.g. Zaroubi 2013). The masses of the AGNs detected at these cosmological distances are higher than $10^{8-9}\,M_{\odot}$ (e.g. Vito et al. 2019), which is indicative of a fast and efficient growth that challenges the standard formation models of supermassive black holes (SMBHs; e.g. Volonteri 2012; Wu et al. 2015). The high-z AGNs that are also radio loud constitute about 10% of the entire AGN population (Bañados et al. 2015; Padovani et al. 2017) and provide a unique opportunity to study the role of jets in the accretion of SMBHs (e.g. Volonteri et al. 2015), their feedback on the host galaxy (e.g. Fabian 2012), and the cosmic evolution of the AGN radio luminosity function (Padovani et al. 2015) out to the largest distances. They can be used as cosmological probes (e.g. Gurvits et al. 1999).

The relativistic jets of radio-loud AGNs called blazars are oriented along the line of sight (Urry & Padovani 1995). Because their non-thermal radiation is relativistically amplified and not obscured along the jet direction, blazars are very bright and visible up to high redshifts, allowing the study of the radio-loud AGNs population throughout cosmic time (e.g. Ajello et al. 2009; Caccianiga et al. 2019). On milliarcsecond scales (probed by very long baseline interferometry, VLBI), blazars usually show an unresolved flat-spectrum component ("core") and a one-sided relatively compact steep-spectrum jet. Moreover, it is possible to measure some physical properties (e.g. the brightness temperature and the bulk Lorentz factor, see Appendix A) of this class of AGN with VLBI (e.g. Lobanov 2010; Lister et al. 2013). Before Belladitta et al. (2020), only seven blazars were known at $z > 5$, the most distant being at $z = 5.47$ (Romani et al. 2004). This is essentially due to the rarity of this type of radio-loud AGN: we estimated $\sim 2 \times 10^{-4}$ blazars every square degree at $z > 5.5$ and with flux densities higher than a few mJy, corresponding to about two to three blazars between $z = 5.5$ and $z = 6.5$ that should be detectable in currently available wide-field surveys (Caccianiga et al. 2019, but see also Padovani et al. 2017).

There is a mismatch of at least an order of magnitude between the number of observed blazars at high redshift and those expected from cosmological models (Haiman et al. 2004; Volonteri et al. 2011). Possible explanations of this large discrepancy include an evolution of the bulk Lorentz factor Γ (decreasing for increasing redshift), a radial velocity structure of the jet (only part of the jet is actually highly beamed), a compact and self-absorbed structure (that prevents the detection at GHz frequencies), and possible observational biases related to strong optical absorption and compact self-absorbed radio emission (Volonteri et al. 2011). In order to clearly assess the origin of this disagreement, detection and confirmation of blazars at large redshifts is urgently required.

By combining the NRAO VLA Sky Survey catalogue (NVSS, Condon et al. 1998, in the radio), the Panoramic Survey Telescope and Rapid Response System (Pan-STARRS PS1, Chambers et al. 2016, in the optical), and the AllWISE Source Catalogue (WISE, Wright et al. 2010; NEOWISE, Mainzer et al. 2011, in the mid-infrared) and using the dropout technique, we discovered PSO J0309+27, which we spectroscopically confirmed to be at a redshift $z = 6.10 \pm 0.03$ (Belladitta et al. 2020). It is the brightest AGN in the radio band discovered to date above redshift 6 (23 mJy as measured with the NVSS). Through a dedicated *Swift*-XRT observation, we measured an X-ray flux of $\sim 3.4 \times 10^{-14}$ erg s^{-1} cm^{-2} in the [0.5−10] keV energy band, which makes PSO J0309+27 also the second brightest AGN in the X-ray band discovered at $z > 6$ (the brightest is CFHQS J142952+544717 from recent SRG/e-ROSITA observations, Medvedev et al. 2020). In addition to the NVSS observation, PSO J0309+27 is also detected in the TIFR GMRT Sky Survey (TGSS, 64.2 ± 6.4 mJy, Intema et al. 2017) at 147 MHz and at 3 GHz by the VLA Sky Survey (VLASS, 12.0 ± 1.2 mJy, Lacy et al. 2019). On the basis of the multi-wavelength observed properties, in particular those at X-ray energies, Belladitta et al. (2020) classified PSO J0309+27 as a blazar.

In this Letter, we present a follow-up of PSO J0309+27 with the VLA and the VLBA, which aims at constraining the radio spectral properties of the target and simultaneously investigates the morphology and physical conditions from arcsec to milliarcsecond (mas) scales, thus unveiling the parsec-scale emission of this high-z AGN. Throughout this Letter, we assume $H_0 = 67.8$ km s^{-1} Mpc^{-1}, $\Omega_M = 0.31$, and $\Omega_\Lambda = 0.69$ (Planck Collaboration XIII 2016). The synchrotron spectral index is defined as $S_\nu \propto \nu^\alpha$. At $z = 6.10 \pm 0.03$, the luminosity distance is 60 132 ± 345 Mpc, which gives a scale of 5.77 ± 0.02 pc mas^{-1}.

2. Observations and data reduction

2.1. VLBA

We observed PSO J0309+27 with the VLBA on 6 April 2020 at central observing frequencies of 1.5, 5, and 8.4 GHz, each with a bandwidth of 512 MHz, and with a 2 Gbps data-recording rate under the Director's Discretionary Time (DDT) project BS294 (PI: Spingola). The observation strategy was that of standard phase referencing, which includes scans on the targets of ∼3.5 min each, interleaved by shorter scans on the phase calibrator (J0316+2733). In the observing run we also included a few scans on DA193 for the bandpass calibration. The total observing time was about 2 h for each band. We systematically cycled through the observing frequencies in the 6 h observation in order to obtain the best possible *uv* coverage at each band. The correlation was performed using the VLBA DiFX correlator in Socorro (Deller et al. 2011).

The data were processed with the Astronomical Image Processing System (AIPS, Greisen 2003) package following the standard VLBA calibration procedure for phase-referenced observations, which we briefly summarise. First, we inspected the visibilities to search for potential bad data (e.g. radio frequency interferences RFIs, and off-source time stamps). Then we corrected for ionospheric dispersive delay, voltage offsets in the samplers, instrumental delay, and parallactic angle variation. We then applied a bandpass calibration and performed the a priori amplitude calibration, which uses gain curves and system temperatures. Finally, a global fringe-fitting run was performed to correct for the residual fringe delays and rates of the calibrator visibilities. The solutions were then interpolated to the target visibilities. We performed several iterations of phase and amplitude self-calibration because the solutions had a sufficient signal-to-noise ratio, until the rms noise limit was reached. The final self-calibrated images at the three observing frequencies are shown in Fig. 1. We adopted a natural weighting scheme to better recover the most diffuse structure of this source at all frequencies. The properties of the images, such as off-source rms noise level, total flux density, peak surface brightness, and restoring beam, are listed in Table B.1.

We fit the observed emission using 2D multi-Gaussian fits to the image-plane using the task `imfit` within the Common Astronomy Software Applications package (CASA, McMullin et al. 2007). The measurements of flux density, peak surface brightness, and sizes obtained using this method are listed in Table B.2, while the identified sub-components are shown in Fig. 2. In addition to the nominal uncertainties of the fit (Table B.2), we consider the uncertainty due to the calibration process (estimated using the scatter on the amplitude gains) to be about 5%.

We obtained synchrotron spectral index maps using images with same pixel size, convolved with the same restoring beam and matched baseline ranges. We have quantified the core-shift effect (Lobanov 1998) between the different frequencies by measuring the position of the core (components 1 or 1a in Table B.2) in the CLEANed images at each band relative to the phase calibrator. This effect must be taken into account when images are aligned at various frequencies to produce spectral index maps. We find that there is no positional offset between the cores at the three frequencies within the astrometric uncertainties (of the order of tens of μas). For the frequency pair 1.5−5 GHz we used the 4−35 $M\lambda$ *uv* range and a circular restoring beam of 13 mas full width at half maximum (FWHM). For the other frequency pair 5−8.4 GHz we used visibilities in the *uv* range of 6−100 $M\lambda$ and a circular restoring beam of 4 mas FWHM. The resulting spectral index images are shown in Fig. 3.

2.2. Jansky VLA

PSO J0309+27 was observed with the *Jansky* VLA (DDT observation, Legacy ID: AB1752, PI: Belladitta) in C configuration on 15 May 2020 from 1.4 to 40 GHz (22 to 0.9 arcsec FWHM), for a total observing time of 1.5 h (50% on source, 50% on calibration). The 1.4 and 2.3 GHz observations used the 8-bit sampler, while the other bands used the 3-bit sampler. Two antennas were excluded from the observations because of technical issues.

Calibration was made using CASA following the standard procedure. We performed imaging (for all bands) and self-calibration (only successful for *L*-, *S*-, *C*-, and *X*-bands) using the AIPS package. The 1.4 and 2.3 GHz observations were most affected by RFIs, causing the loss of a few spectral windows (spws). We obtained separate images for each spw from 1.4 to 15 GHz using natural weights, while we averaged the 64 spws in chunks of 8 spws from 15 to 40 GHz to maximise the sensitivity. From these images we extracted the flux density of the source (unresolved at all frequencies) using a 2D Gaussian fit, and we obtained a broad-band radio spectrum from 1.4 to 40 GHz for PSO J0309+27, which is shown in Fig. 4. The measurements are reported in Table B.3. In addition to the nominal uncertainties provided by the fit (reported in Table B.3), we consider the uncertainty due to the calibration process (estimated using the scatter on the amplitude gains) to be about 3−5% from 1.4 to 15 GHz, and it is about 10−15% at 15 and 40 GHz.

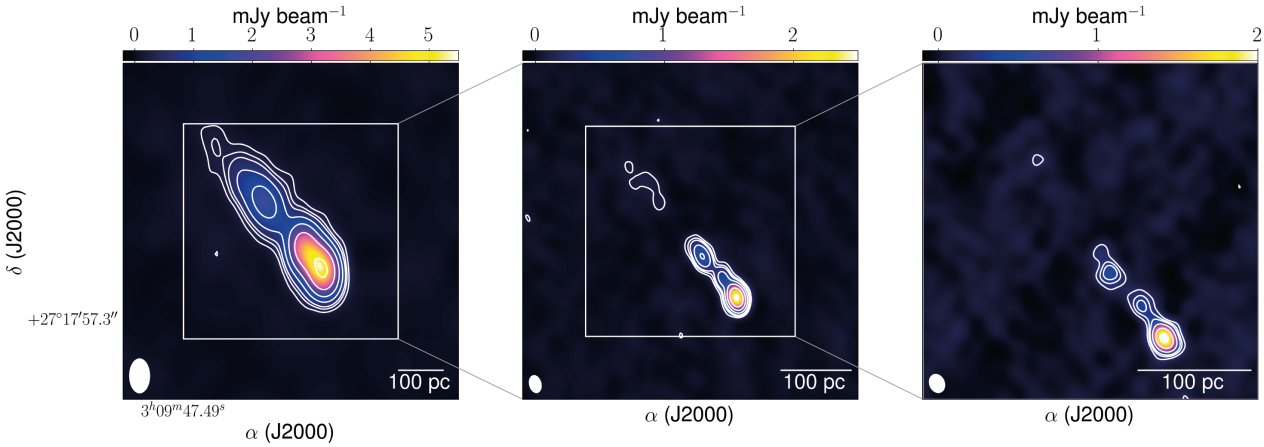

Fig. 1. Self-calibrated images of PSO J0309+27 at 1.5 GHz (*left*), 5 GHz (*centre*), and 8.4 GHz (*right*). The contours are drawn at (−3, 3, 6, 9, 18, 36, 72, and 144) times the off-source noise of each map, which are given in Table B.1. The white colour bar indicates 100 pc in projection at $z = 6.1$. The restoring Gaussian beam is shown in white in the bottom left corner of each image; north is up, and east is left.

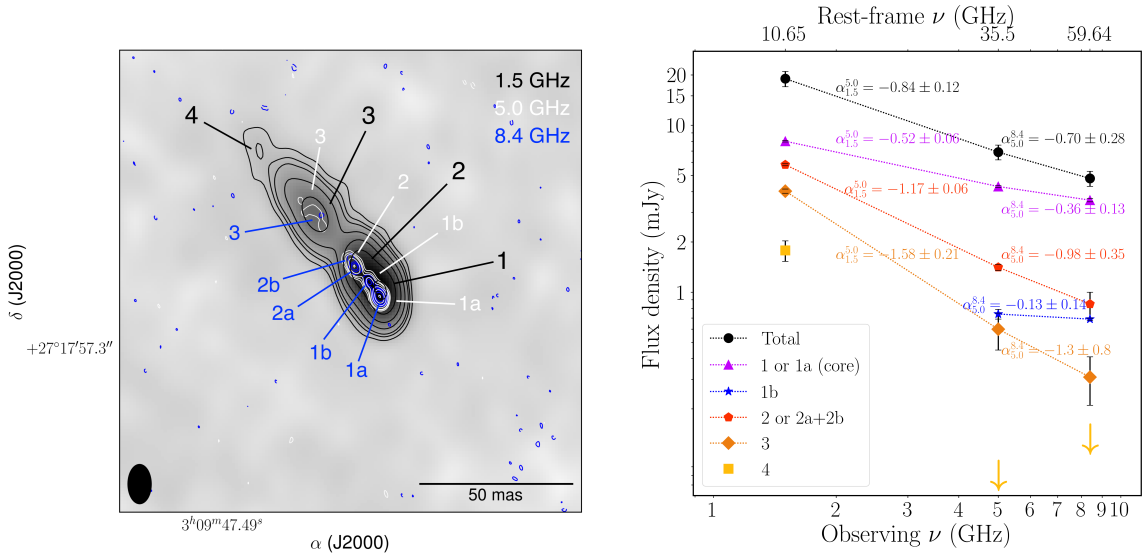

Fig. 2. *Left*: overlay of the 1.5 (black contours), 5 (white contours), and 8.4 GHz (blue contours) emission of PSO J0309+27. The greyscale map is the 1.5 GHz self-calibrated image, and its restoring beam is shown in the bottom left corner; north is up, and east is left. The phased referenced absolute position of component 1a is 03^{h}09^{m}47.4862^s, +27°17′57.3165″. *Right*: radio spectrum of all the sub-components of PSO J0309+27 spatially resolved by the multi-frequency VLBI observations presented here. We indicate the 3σ detection limit for sub-component 4 at 5 and 8.4 GHz with arrows, estimated as three times the flux density within the same area of the 1.5 GHz detection of that sub-component.

3. Results

3.1. Spatially resolved multi-frequency radio emission

On VLBI scales, PSO J0309+27 is a core plus one-sided jet from 1.5 to 8.4 GHz (see Fig. 1). The jet extends at 1.5 GHz for about 80 mas at a position angle 30° (east of north), which corresponds to ∼500 pc at the redshift of the source. At this frequency, it is resolved into four steep-spectrum sub-components that are connected by continuous emission (Fig. 2, but see also Sect. 3.2). At 1.5 GHz, we recover only ∼85% of the flux density measured by the NVSS. This can be taken as an indication for possible extended structure on scales that are resolved out by our VLBI observations. Nevertheless, this difference in flux density might also be due to intrinsic variability, as suggested by the comparison between our *Jansky* VLA data from May 2020 at 1.5 GHz (22 arcsec FWHM, flux density of 30 mJy) and what was measured by the NVSS in 1993 (45 arcsec FWHM, flux density of about 24 mJy; see also Fig. 4 and Sect.3.2).

At 5 and 8.4 GHz, we spatially resolve the core (component 1 at 1.5 GHz) into two sub-components (1a and 1b) and the jet into three sub-components (Figs. 1 and 2). At these frequencies we do not detect jet sub-component 4 (clearly detected at 1.5 GHz), which may be due to its intrinsically low surface brightness and steep synchrotron spectral index. The radio core (1a) dominates the radio emission at 5 and 8.4 GHz, it contributes about 60% of the total integrated flux density at both bands (see Appendix B).

At all the three frequencies, the jet decrease between components 2 and 3 (see Figs. 1 and 2). This resembles a recollimation region immediately after knot 1b (Hervet et al. 2017; Bodo & Tavecchio 2018; Nishikawa et al. 2020). Similar jet recollimations have been observed in other AGN jets in the local Universe (e.g. Giroletti et al. 2012; Asada et al. 2014;

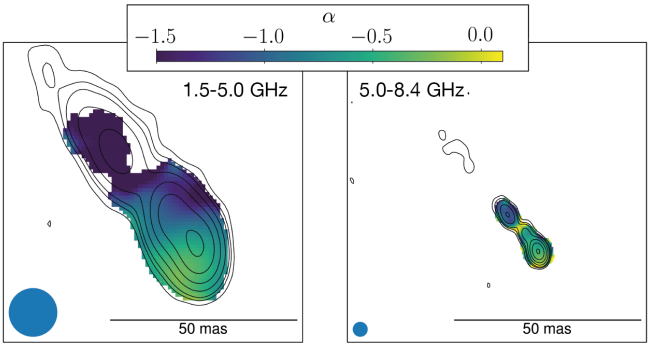

Fig. 3. Spectral index maps of PSO J0309+27 ($S_\nu \propto \nu^\alpha$) for the frequency pairs 1.5−5.0 GHz (*left*) and 5.0−8.4 GHz (*right*). The black contours are the 1.5 GHz emission on the left, and the 5 GHz emission on the right, with the same increasing scheme as Fig. 1. The circular restoring beam is 13 mas FWHM (1.5−5.0 GHz image) and 4 mas FWHM (5.0−8.4 GHz image), and it is shown in the bottom left corner of each map.

Hada et al. 2018; Nakahara et al. 2019) and at high redshift (e.g. Frey et al. 2015).

Finally, we do not find evidence for any emission that could be associated with a possible lensed image of PSO J0309+27. Gravitational lensing can strongly amplify the intrinsic luminosity of an AGN, and it therefore has a crucial role in assessing the intrinsic properties of sources (e.g. Spingola & Barnacka 2020; Spingola et al. 2020). We searched for possible lensed images in an area of 3 arcsec^2, which is the largest region not affected by bandwidth and time smearing. If gravitationally lensed, the system should more likely consist of a doubly imaged source because there is no detection of a mirror symmetric emission that can be attributed to a merging image of a quadruply imaged lens system (Fig. 1). By assuming a flux density ratio ≤15:1 and a minimum angular separation of 100 mas (e.g. Spingola et al. 2019), the second lensed image is expected to have a flux density of about 1.3 mJy at 1.5 GHz. Therefore, if present in the area, such lensed image should be detected at 30σ level.

3.2. Radio spectrum

The spectral index is a fundamental parameter in the study of AGN jets because it allows us to clearly separate the optically thick base of the jet (the "core"), which is closest to the SMBH, from the steep-spectrum components associated with the more external part of the radio jets. In Fig. 2 (right panel) we show the radio spectrum for all of the sub-components of PSO J0309+27 that we resolved using VLBI (see the left panel of Fig. 2 for the labels). We can identify the brightest component (1 or 1a) as the radio core region because it shows a flatter synchrotron spectral index between 1.5 and 5 GHz than the other sub-components ($\alpha = -0.52 \pm 0.06$, see Eq. (A.1)). Moreover, its spectral index becomes flatter between 5 and 8.4 GHz, as we resolve it into two sub-components (1a and 1b). Nevertheless, our 2D Gaussian fit does not associate component 1a with a point-like source, indicating that the actual source radio core is blended with the innermost optically thick part of the jet. Component 1b also shows a flat spectrum between 5 and 8.4 GHz, and it is one of the faintest sub-components. All of the other sub-components have a steep spectral index α, with values between -1.58 ± 0.21 and -0.98 ± 0.35, but the uncertainties on the integrated flux density for some of them are quite large. The most external jet component (labelled 4) is undetected at 5 and 8.4 GHz, as described in Sect. 3.1.

Spectral index maps for each frequency pair are shown in Fig. 3. There is a clear spectral index gradient between the core (flatter α) and the jet (steeper α). The most external jet components are clearly the steepest in PSO J0309+27, which is consistent with what is usually observed in radio-loud AGNs at all redshifts (Blandford et al. 2019).

The broad-band radio spectrum as measured by the VLA (shown in Fig. 4) is consistent with the steep-spectrum trend measured with the VLBA. By fitting the VLA data with a single power-law model, we find a spectral index of $\alpha = -0.98 \pm 0.05$ between 1 and 40 GHz. The spectrum from the 15 GHz data also shows indications of steepening (Fig. 4), therefore we also fit the VLA observations using a broken power law, which finds a break at $\nu_{\rm break} = 14.5 \pm 0.5$ GHz (rest frame 103 GHz), a spectral index of $\alpha = -0.96 \pm 0.03$ before $\nu_{\rm break}$ and $\alpha = -1.39 \pm 0.09$ after $\nu_{\rm break}$. The single and broken power-law models both represent the data well; they have similar reduced chi-square values (1.8 and 2.2, respectively). This is also shown in Fig. 4: both fits are consistent with the observations within the uncertainties.

By comparing the VLA data at 1.4 and 3 GHz with the archival observations of NVSS (at 1.4 GHz in 1993) and VLASS (at 3 GHz in 2017), we find an indication for a 20−30% variability in this source. This type of a 20−30% variability on scales of several months to a few years[1] in the radio has been observed in other radio-loud AGNs, but we cannot exclude that PSO J0309+27 had a much more pronounced variability on shorter timescales, which is typical of blazars (e.g. Hovatta et al. 2008). Future long-term monitoring is needed to assess the amplitude and timescale of the variability in this AGN.

Moreover, we observe a flattening of the spectrum at low frequencies (between 0.147 and 1.4 GHz, Fig. 4). Therefore, the spectral turnover must be at low frequencies because the flux density at 147 MHz is higher than at 1.4 GHz (Fig. 4).

3.3. Physical properties

In the VLBI images we do not find any evidence for a counter-jet, which indicates that this AGN is seen under a relatively small viewing angle, as expected if PSO J0309+27 is a blazar (Belladitta et al. 2020). To estimate the possible ranges of viewing angles θ and of the bulk velocity in terms of speed of light ($\beta_{\rm bulk}$), it is possible to use the ratio of jet to counter-jet brightness J (Giovannini et al. 1994, see Eq. (A.2)). We used the 5 GHz observation because it is the most sensitive of our VLBA observations, we assumed the 1σ off-source noise level as an upper limit for the counter-jet surface brightness and adopted a synchrotron spectral index of component 1a of between 1.5 and 5 GHz (Fig. 2). We find a minimum bulk velocity $\beta^{\rm bulk}_{\rm min}$ of 0.78 and a maximum viewing angle $\theta_{\rm max}$ of 38°, as shown in Fig. 5. An independent way to estimate θ and the β is given by the core dominance correlation (Giovannini et al. 1988, 1994; Giroletti et al. 2004). We used the 5 GHz flux density of the core measured from our VLBA observations (4.3 mJy) and estimated the total 408 MHz flux density using a spectral index of $\alpha = -0.98 \pm 0.05$, which is the best-fitting value for the total spectral index between 1 and 40 GHz using a single power-law model (Sect. 3.2). We account for a 30% variability of the core and the scatter of the relation, finding a small range of allowed values

[1] The rest-frame time difference between the NVSS and VLASS observations is $\Delta t \simeq 3.4$ years, and that between the VLASS and our VLA observations is $\Delta t \simeq 0.4$ years.

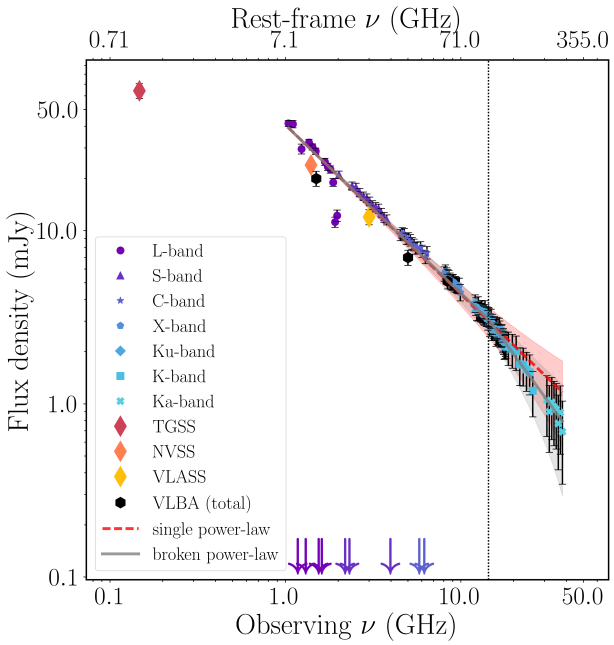

Fig. 4. Radio spectrum of PSO J0309+27 from 0.147 up to 40 GHz. The VLA observations from 1.4 to 40 GHz are represented with different symbols for each band as indicated in the legend (bottom left corner). Archival TGSS, NVSS, and VLASS observations are indicated with diamonds, while the total flux density of the VLBA observations is reported as filled black hexagons. The arrows indicate flagged spws. The red (dashed) and grey (solid) lines stand for the single and broken power-law fits, respectively, where the shaded areas represent the uncertainties of the fits (same colour coding). The vertical dotted line indicates the frequency break of the broken power-law fit (14.5 GHz).

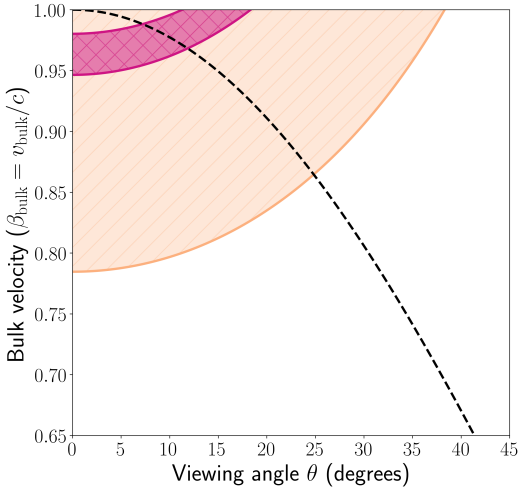

Fig. 5. Allowed values of the jet viewing angle (θ) and its bulk velocity ($v_{\rm bulk}$) in units of the speed of light ($\beta_{\rm bulk} = v_{\rm bulk}/c$). The hatched orange area corresponds to the allowed parameter space in the β–θ plane using the ratio of jet to counter-jet brightness, and the magenta area traces the parameter space allowed by the correlation of Giovannini et al. (1988), as explained in Sect. 3.3. The dashed black line corresponds to $1/\Gamma$, which is the typical value to discern between aligned ($<1/\Gamma$) and misaligned ($>1/\Gamma$) AGN.

well within the constraints from J (shown in Fig. 5). Because this relation was obtained for a sample of local radio galaxies, this range is only indicative and not definitive.

By assuming $\beta_{\rm min}^{\rm bulk}$ and $\theta_{\rm max}$, we find a minimum Lorentz factor $\Gamma_{\rm min} \simeq 1.59$ and a minimum Doppler factor $\delta_{\rm min} \simeq 1.62$ (see Eqs. (A.3) and (A.4)). These values for the lower limits on Γ and δ are among the lowest values observed in blazars (e.g. Hovatta et al. 2009; Li et al. 2020). Nevertheless, we highlight that they were estimated using the maximum viewing angle ($\theta_{\rm max}$) constrained by the VLBI data, which is a (shallow) upper limit on the true viewing angle of PSO J0309+27.

We estimate the source-frame brightness temperature of each sub-component (Eq. (A.5)), and the values of $T_{\rm B}$ are reported in Table B.2. The brightness temperature of the sub-components of PSO J0309+27 is of the order of 10^8 K at 1.5 and 5 GHz, and 10^7 K at 8.4 GHz. We find a broad trend of decreasing $T_{\rm B}$ as a function of increasing observing frequency for all of the components (Lee 2014). We highlight that the rest-frame emitting frequencies are quite high; they are 10.7, 35.5, and 59.6 GHz at 1.5, 5, and 8.4 GHz, respectively.

Because the energy density of the CMB scales as $\propto(1+z)^4$, the inverse Compton scattering on the CMB photons (iC-CMB) is expected to play an important role at the redshift of PSO J0309+27 (Tavecchio et al. 2000; Schwartz 2002; Ghisellini et al. 2014). Using the ratio between the radio luminosity of the jet and the X-ray luminosity (Appendix A, making the assumption that the X-ray emission is due to the jet only and using the radio luminosity of the jet without the core, Table B.2), we find a magnetic field of $H_{\rm iC} \sim 0.09$ mG. This assumption is supported by the high X-ray luminosity of this AGN (Belladitta et al. 2020), which exceeds the expectations for radio-quiet AGNs by far (e.g. Miller et al. 2011).

This value is significantly lower that what has been derived by assuming equipartition conditions ($H_{\rm eq} \sim 4$ mG) and the equivalent magnetic field of the CMB at $z = 6.1$ ($H_{\rm CMB} \sim 0.17$ mG). In general, iC-CMB is more efficient than synchrotron in cooling the electrons if $H_{\rm CMB} > H_{\rm eq}$. In addition, *Swift*-XRT observations do not spatially resolve the X-ray emission, which may be much more extended than the VLBI jet component. Therefore it is possible that the jet is significantly affected by iC-CMB on the X-ray scales (e.g. Worrall et al. 2020). Because we also find that $H_{\rm eq} > H_{\rm CMB}$, however, the energy losses within the radio jet are probably dominated by synchrotron, and the iC-CMB contribution is negligible.

4. Discussion and conclusions

We reported the analysis of the morphology and physical properties of PSO J0309+27, which is spatially resolved on parsec scales for the first time by our DDT follow-up radio observations. With the sensitive VLBA observations, we unveil a bright jet extended on ~500 parsecs in projection, which is resolved into multiple sub-components (Fig. 1).

We find brightness temperature values of $\sim 10^8$ K. Similar values for $T_{\rm B}$ associated with bright extended steep-spectrum jets (from a few to hundreds of parsecs in projection) have also been measured in other radio-loud AGNs at redshifts $z > 4$ (Frey et al. 2011; Gabanyi et al. 2015; Cao et al. 2017; Bañados et al. 2018; Zhu 2018; Momjian et al. 2018; An et al. 2020, but see Frey et al. 2015 for higher $T_{\rm B}$ values at $z \sim 5$). These $T_{\rm B}$ estimates are two to three orders of magnitudes lower than what has been measured for the blazar sample of MOJAVE observed at 15 GHz (Kovalev et al. 2005; Homan et al. 2006; at redshifts up to $z \simeq 3.5$, Cara & Lister 2008), and the VLBA-BU-BLAZAR sample observed at 43 GHz (at redshifts up to $z \simeq 2.5$, Jorstad & Marscher 2016; Jorstad et al. 2017). Moreover, the lower values of $T_{\rm B}$ in PSO J0309+27 are explained by

the frequency dependence of T_B (Lee 2014), by the location of the turnover of the synchrotron emission in the MHz regime (rest frame 1−7 GHz, Fig. 4), and by the very high rest-frame frequencies sampled by the observations (∼7−300 GHz, Fig. 4).

Another issue in the estimate of the Doppler factor and T_B is related to the single-epoch measurement. Such estimates from a single-epoch observation are usually much lower than what is derived from variability (e.g. Orienti et al. 2015) because variability may overcome the intrinsic limitations due to the angular resolution of the instrument and can probe much smaller emitting regions simply because of causality arguments.

Our derived values for the magnetic field in PSO J0309+27 indicate that the iC-CMB process is negligible within the radio jet detected on VLBI-scales, while it could be important for the X-ray emission.

Overall, the physical properties of this AGN at redshift z = 6.1 point to a moderately beamed jet (Sect. 3.3 and Table B.2). However, the observational constraints we derived from a single-epoch observation are too loose to obtain stringent values for parameters such as the bulk velocity and the viewing angle of the jet, so that we are able mainly to place upper (or lower) limits. Nevertheless, if PSO J0309+27 is a blazar, as suggested by its X-ray properties (Belladitta et al. 2020), then in Fig. 5 it should lie below the dashed line, which is the typical value to discern between aligned ($<1/\Gamma$) and misaligned ($>1/\Gamma$) AGNs, and below the maximum value allowed by the core-dominance relation (that is $\beta_{\rm bulk}$ = 0.98). This implies a Lorentz factor Γ of ≃5 or lower (using Eq. (A.3)). A value of Γ of ≃5 would agree very well with what has been proposed by Volonteri et al. (2011) to reconcile the significant deficit of observed high-z blazars with respect to the expected number of blazars at $z \gtrapprox 3$.

Finally, we highlight that our findings cannot exclude the possibility that PSO J0309+27 is seen under a larger viewing angle. In this case, the values for Γ could be higher, but the bright X-ray emission would need a boost, which could be due to iC-CMB scattering. More stringent constraints on the bulk Lorentz factor in PSO J0309+27 and on the other high-z blazars are necessary to test whether Γ is intrinsically low in distant blazars and does change as a function of redshift.

Acknowledgements. We thank the anonymous referee for their constructive comments to the manuscript. CS thanks the NRAO analysts for their prompt help with the preparation of the schedule and delivery of the data during the critical period of April–May 2020 due to the COVID-19 pandemic. The authors are grateful to Leonid Gurvits and Alexey Melnikov for providing information on the Russian VLBI-network "Quasar" observations of this target and the useful discussions on this work. CS is grateful for support from the National Research Council of Science and Technology, Korea (EU-16-001). The National Radio Astronomy Observatory is a facility of the National Science Foundation operated under cooperative agreement by Associated Universities, Inc. This research made use of APLpy, an open-source plotting package for Python (Robitaille & Bressert 2012).

References

Ajello, M., Costamante, L., Sambruna, R. M., et al. 2009, ApJ, 699, 603
An, T., Mohan, P., Zhang, Y., et al. 2020, Nat. Commun., 11, 143
Asada, K., Nakamura, M., Doi, A., Nagai, H., & Inoue, M. 2014, ApJ, 781, L2
Bañados, E., Venemans, B. P., Morganson, E., et al. 2015, ApJ, 804, 118
Bañados, E., Carilli, C., Walter, F., et al. 2018, ApJ, 861, L14
Belladitta, S., Moretti, A., Caccianiga, A., et al. 2020, A&A, 635, L7
Blandford, R., Meier, D., & Readhead, A. 2019, ARA&A, 57, 467
Bodo, G., & Tavecchio, F. 2018, A&A, 609, A122
Caccianiga, A., Moretti, A., Belladitta, S., et al. 2019, MNRAS, 484, 204
Cao, H. M., Frey, S., Gabányi, K. É., et al. 2017, MNRAS, 467, 950
Cara, M., & Lister, M. L. 2008, ApJ, 674, 111
Chambers, K. C., Magnier, E. A., Metcalfe, N., et al. 2016, ArXiv e-prints [arXiv:1612.05560]
Condon, J. J., Cotton, W. D., Greisen, E. W., et al. 1998, AJ, 115, 1693
Deller, A. T., Brisken, W. F., Phillips, C. J., et al. 2011, PASP, 123, 275
Fabian, A. C. 2012, ARA&A, 50, 455
Fixsen, D. J. 2009, ApJ, 707, 916
Frey, S., Paragi, Z., Gurvits, L. I., Gabányi, K. É., & Cseh, D. 2011, A&A, 531, L5
Frey, S., Paragi, Z., Fogasy, J. O., & Gurvits, L. I. 2015, MNRAS, 446, 2921
Gabanyi, K. E., Cseh, D., Frey, S., et al. 2015, MNRAS, 450, L57
Ghisellini, G., Celotti, A., Tavecchio, F., Haardt, F., & Sbarrato, T. 2014, MNRAS, 438, 2694
Giovannini, G., Feretti, L., Gregorini, L., & Parma, P. 1988, A&A, 199, 73
Giovannini, G., Feretti, L., Venturi, T., et al. 1994, ApJ, 435, 116
Giroletti, M., Giovannini, G., Feretti, L., et al. 2004, ApJ, 600, 127
Giroletti, M., Hada, K., Giovannini, G., et al. 2012, A&A, 538, L10
Greisen, E. W. 2003, in AIPS, the VLA, and the VLBA, ed. A. Heck, Astrophys. Space Sci. Lib., 285, 109
Gurvits, L. I., Kellermann, K. I., & Frey, S. 1999, A&A, 342, 378
Hada, K., Doi, A., Wajima, K., et al. 2018, ApJ, 860, 141
Haiman, Z., Quataert, E., & Bower, G. C. 2004, ApJ, 612, 698
Hervet, O., Meliani, Z., Zech, A., et al. 2017, A&A, 606, A103
Homan, D. C., Kovalev, Y. Y., Lister, M. L., et al. 2006, ApJ, 642, L115
Hovatta, T., Nieppola, E., Tornikoski, M., et al. 2008, A&A, 485, 51
Hovatta, T., Valtaoja, E., Tornikoski, M., & Lähteenmäki, A. 2009, A&A, 494, 527
Intema, H. T., Jagannathan, P., Mooley, K. P., & Frail, D. A. 2017, A&A, 598, A78
Jorstad, S., & Marscher, A. 2016, Galaxies, 4, 47
Jorstad, S. G., Marscher, A. P., Morozova, D. A., et al. 2017, ApJ, 846, 98
Kovalev, Y. Y., Kellermann, K. I., Lister, M. L., et al. 2005, AJ, 130, 2473
Lacy, M., Chandler, C., Kimball, A., et al. 2019, in Astronomical Data Analysis Software and Systems XXVII, eds. P. J. Teuben, M. W. Pound, B. A. Thomas, & E. M. Warner, ASP Conf. Ser., 523, 217
Lee, S.-S. 2014, J. Korean Astron. Soc., 47, 303
Li, X., An, T., Mohan, P., & Giroletti, M. 2020, ApJ, 896, 63
Lister, M. L., Aller, M. F., Aller, H. D., et al. 2013, AJ, 146, 120
Lobanov, A. P. 1998, A&AS, 132, 261
Lobanov, A. 2010, ArXiv e-prints [arXiv:1010.2856]
Mainzer, A., Grav, T., Masiero, J., et al. 2011, EPSC-DPS Joint Meeting 2011, 2011, 1530
McMullin, J. P., Waters, B., Schiebel, D., Young, W., & Golap, K. 2007, in Astronomical Data Analysis Software and Systems XVI, eds. R. A. Shaw, F. Hill, & D. J. Bell, ASP Conf. Ser., 376, 127
Medvedev, P., Sazonov, S., Gilfanov, M., et al. 2020, MNRAS, 497, 1842
Miller, B. P., Brandt, W. N., Schneider, D. P., et al. 2011, ApJ, 726, 20
Momjian, E., Carilli, C. L., Bañados, E., Walter, F., & Venemans, B. P. 2018, ApJ, 861, 86
Nakahara, S., Doi, A., Murata, Y., et al. 2019, ApJ, 878, 61
Nishikawa, K., Mizuno, Y., Gómez, J. L., et al. 2020, MNRAS, 493, 2652
Orienti, M., D'Ammando, F., Larsson, J., et al. 2015, MNRAS, 453, 4037
Pacholczyk, A. G. 1970, Radio Astrophysics. Nonthermal Processes in Galactic and Extragalactic Sources (San Francisco: Freeman)
Padovani, P., Bonzini, M., Kellermann, K. I., et al. 2015, MNRAS, 452, 1263
Padovani, P., Alexander, D. M., Assef, R. J., et al. 2017, A&ARv, 25, 2
Planck Collaboration XIII. 2016, A&A, 594, A13
Robitaille, T., & Bressert, E. 2012, Astrophysics Source Code Library [record ascl:1208.017]
Romani, R. W., Sowards-Emmerd, D., Greenhill, L., & Michelson, P. 2004, ApJ, 610, L9
Schwartz, D. A. 2002, ApJ, 571, L71
Spingola, C., & Barnacka, A. 2020, MNRAS, 494, 2312
Spingola, C., McKean, J. P., Lee, M., Deller, A., & Moldon, J. 2019, MNRAS, 483, 2125
Spingola, C., McKean, J. P., Vegetti, S., et al. 2020, MNRAS, 495, 2387
Tavecchio, F., Maraschi, L., Sambruna, R. M., & Urry, C. M. 2000, ApJ, 544, L23
Urry, C. M., & Padovani, P. 1995, PASP, 107, 803
Vito, F., Brandt, W. N., Bauer, F. E., et al. 2019, A&A, 630, A118
Volonteri, M. 2012, Science, 337, 544
Volonteri, M., Haardt, F., Ghisellini, G., & Della Ceca, R. 2011, MNRAS, 416, 216
Volonteri, M., Silk, J., & Dubus, G. 2015, ApJ, 804, 148
Worrall, D. M., Birkinshaw, M., Marshall, H. L., et al. 2020, MNRAS, 497, 988
Wright, E. L., Eisenhardt, P. R. M., Mainzer, A. K., et al. 2010, AJ, 140, 1868
Wu, X.-B., Wang, F., Fan, X., et al. 2015, Nature, 518, 512
Zaroubi, S. 2013, in The Epoch of Reionization, eds. T. Wiklind, B. Mobasher, & V. Bromm, Astrophys. Space Sci. Lib., 396, 45
Zhu, S. 2018, Am. Astron. Soc. Meet. Abstr., 231, 123.06

Appendix A: Derivation of physical parameters

We adopt the definition of synchrotron spectral index α as $S_\nu \propto \nu^\alpha$, where S_ν is the flux density at the observing frequency ν. The uncertainty on the spectral index (σ_α) between two frequencies ν_1 and ν_2 is given by

$$\sigma_\alpha = \frac{1}{\ln(\nu_1/\nu_2)} \sqrt{\left(\frac{\sigma_{S_{\nu_1}}}{S_{\nu_1}}\right)^2 + \left(\frac{\sigma_{S_{\nu_2}}}{S_{\nu_2}}\right)^2}, \tag{A.1}$$

where $\sigma_{S_{\nu_1}}$ and $\sigma_{S_{\nu_2}}$ are the uncertainties on the flux densities measured at the frequencies ν_1 and ν_2.

To estimate the possible ranges of viewing angles θ and of the bulk velocity in terms of the speed of light $\beta_{\rm bulk}$, it is possible to use the ratio of the jet to the counter-jet (J) brightness,

$$\beta_{\rm bulk} \cos(\theta) = (J^{1/p} - 1)/(J^{1/p} + 1), \tag{A.2}$$

where $p = 2 - \alpha$ assuming continuous and symmetric jets (e.g. Giovannini et al. 1994) and α is the synchrotron spectral index of component 1a between 1.5 and 5 GHz (Fig. 2). The Lorentz factor is related to the bulk velocity $\beta_{\rm app}$ as

$$\Gamma = (1 - \beta_{\rm bulk}^2)^{-1/2}, \tag{A.3}$$

and the Doppler factor δ is related to Γ via

$$\delta = [\Gamma(1 - \beta \cos\theta)]^{-1}. \tag{A.4}$$

The source-frame brightness temperature is defined as

$$T_{\rm B}(\lambda) = \frac{2 \ln 2}{\pi \kappa} \frac{S_\lambda \lambda^2 (1+z)}{\theta_{\rm maj} \theta_{\rm min}} \, [{\rm K}], \tag{A.5}$$

where κ is the Boltzmann constant, S_λ is the integrated flux density of each sub-component at the observing wavelength λ, z is the redshift, and $\theta_{\rm maj}$ and $\theta_{\rm min}$ are the FWHMs of the elliptical 2D Gaussian fits along the major and the minor axes, all in cgs units (e.g. Kovalev et al. 2005).

By assuming that the contributions of the magnetic field and the relativistic particles are equal (Pacholczyk 1970), it is possible to estimate the so-called equipartition magnetic field as

$$H_{\rm eq} = \left(4.5 \, (1+\eta) \, c_{12} \, \frac{L}{V}\right)^{2/7} \, [{\rm G}], \tag{A.6}$$

where we assumed $\eta = 1$, meaning that proton and electron energies are assumed to be the same, c_{12} is a constant with a value of 3.9×10^7, V is the volume of the radio-emitting source in cm^3 (that we assumed to be homogeneously filled by relativistic plasma), and L is the bolometric radio luminosity (erg s^{-1}) between $\nu_1 = 10$ MHz and $\nu_2 = 100$ GHz, defined as

$$L = 4\pi D_{\rm L}^2 \, (1+z)^{-(1+\alpha)} \int_{\nu_1}^{\nu_2} S_0 \left(\frac{\nu}{\nu_0}\right)^\alpha \, {\rm d}\nu, \tag{A.7}$$

where $D_{\rm L}$ is the luminosity distance, z is the redshift, and S_0 is the flux density at the observing frequency ν_0.

The ratio between the radio (due to synchrotron, $L_{\rm radio}$) and X-ray (due to inverse Compton scattering, $L_{\rm X\text{-}rays}$) luminosities can also give an estimate of the magnetic field H (Schwartz 2002),

$$\frac{L_{\rm radio}}{L_{\rm X\text{-}ray}} = \frac{H^2/8\pi}{\rho_{\rm CMB}}, \tag{A.8}$$

where $\rho_{\rm CMB} = 7.56 \times 10^{-15} T_0^4 \, (1+z)^4$ (erg cm^{-3}) is the energy density of the CMB, and $T_0 = 2.7255$ K is the value of the CMB temperature today (Fixsen 2009).

The equivalent magnetic field at a redshift z due to the CMB can be estimated following Ghisellini et al. (2014),

$$B_{\rm CMB} = 3.26 \times 10^{-6} \, (1+z)^2 \, [{\rm G}]. \tag{A.9}$$

Appendix B: VLA and VLBA observation properties

In this section, we report the parameters of the self-calibrated VLBA images (Table B.1), the properties of the VLBI sub-components (Table B.2), and the VLA measurements (Table B.3).

Table B.1. Properties of the self-calibrated VLBA images of PSO J0309+27 shown in Fig. 1.

Freq. (GHz)	Total flux density (mJy)	Peak surface brightness (mJy beam^{-1})	rms (μJy beam^{-1})	$B_{\rm maj}$ (mas)	$B_{\rm min}$ (mas)	$B_{\rm PA}$ (deg)
1.5	20 ± 2	7.2 ± 0.7	42	12.8	7.6	0
5.0	7.0 ± 0.7	4.1 ± 0.4	25	4.2	2.9	14
8.4	5.1 ± 0.5	3.2 ± 0.3	43	2.8	2.3	23

Notes. The table lists: observing frequency (Col. 1), total integrated flux density (Col. 2), peak surface brightness (Col. 3), off-source rms noise (Col. 4), major and minor axes of the Gaussian restoring beam (Cols. 5 and 6), and the position angle (Col. 7, east of north).

Table B.2. Spatially resolved radio properties of PSO J0309+27 obtained using 2D Gaussian fitting.

Frequency (GHz)	Component	Peak surface brightness (mJy beam^{-1})	Integrated flux density (mJy)	$\theta_{\rm maj}$ (mas)	$\theta_{\rm min}$ (mas)	$T_{\rm B}$ (10^8 K)
1.5 (10.65)	1 (core)	6.83 ± 0.04	8.02 ± 0.08	13.6 ± 0.1	8.3 ± 0.1	2.7 ± 0.2
	2	4.82 ± 0.04	5.80 ± 0.08	13.6 ± 0.2	8.6 ± 0.1	1.9 ± 0.2
	3	1.98 ± 0.04	4.03 ± 0.12	19.2 ± 0.5	10.3 ± 0.5	0.8 ± 0.1
	4	0.30 ± 0.04	1.78 ± 0.25	20.5 ± 0.5	16.1 ± 1.1	0.2 ± 0.1
5 (35.5)	1a (core)	4.18 ± 0.03	4.29 ± 0.05	4.2 ± 0.1	2.9 ± 0.1	>1.19
	1b	0.70 ± 0.03	0.74 ± 0.05	4.2 ± 0.2	2.9 ± 0.1	>0.20
	2	1.02 ± 0.03	1.41 ± 0.06	5.4 ± 0.2	3.0 ± 0.1	0.30 ± 0.02
	3	0.12 ± 0.03	0.60 ± 0.15	12.3 ± 3.1	4.9 ± 0.9	0.03 ± 0.01
8.4 (59.64)	1a (core)	3.21 ± 0.04	3.55 ± 0.08	2.8 ± 0.1	2.3 ± 0.1	>0.67
	1b	0.46 ± 0.04	0.69 ± 0.10	4.4 ± 0.6	2.3 ± 0.2	0.09 ± 0.01
	2a	0.55 ± 0.04	0.71 ± 0.09	3.1 ± 0.3	2.6 ± 0.2	0.11 ± 0.02
	2b	0.23 ± 0.04	0.14 ± 0.05	2.3 ± 0.5	2.0 ± 0.3	0.04 ± 0.02

Notes. The table lists: observing (and rest-frame in parentheses) frequency in GHz (Col. 1); sub-component identification as labelled in Fig. 2 (Col. 2); peak surface brightness in mJy beam^{-1} (Col. 3); integrated flux density in mJy (Col. 4); elliptical size convolved by the beam, i.e. major and minor axes ($\theta_{\rm maj}$ and $\theta_{\rm min}$) in mas (Cols. 5 and 6); rest-frame brightness temperature $T_{\rm B}$ in units of 10^8 K (Col. 7). If the subcomponent is unresolved, then we provide only lower limits on its $T_{\rm B}$ (indicated by >).

Table B.3. Observing frequency (Col. 1), flux density (Col. 2), and nominal uncertainty on flux density from the 2D Gaussian fit (Col. 3) of PSO J0309+27 measured from the VLA observations (Sect. 2 and Fig. 4).

ν (GHz)	S_ν (mJy)	σ_{S_ν} (mJy)	ν (GHz)	S_ν (mJy)	σ_{S_ν} (mJy)
1.040	41.61	0.75	12.082	3.81	0.07
1.104	41.25	1.47	12.203	3.66	0.07
1.170	*flagged*		12.331	3.44	0.07
1.237	29.65	1.50	12.459	3.43	0.07
1.298	*flagged*		12.587	3.71	0.07
1.362	32.26	0.63	12.716	3.46	0.07
1.424	30.42	0.28	12.843	3.46	0.07
1.487	28.75	0.30	12.971	3.39	0.07
1.541	*flagged*		13.099	3.53	0.07
1.604	*flagged*		13.227	3.37	0.07
1.679	24.97	0.32	13.355	3.34	0.06
1.744	23.38	0.29	13.476	3.29	0.06
1.807	22.56	0.29	13.618	3.23	0.06
1.872	19.01	0.27	13.739	3.51	0.06
1.917	11.21	0.15	13.867	3.33	0.06
1.974	12.22	0.49	13.995	3.20	0.06
2.022	21.00	0.21	14.123	3.22	0.06
2.179	*flagged*		14.251	3.06	0.07
2.307	*flagged*		14.379	3.20	0.06
2.396	18.10	0.18	14.507	3.16	0.06
2.527	17.82	0.18	14.635	2.83	0.06
2.655	16.59	0.17	14.763	2.92	0.06
2.783	15.81	0.17	14.891	3.12	0.06
2.911	15.39	0.16	15.012	2.69	0.07
3.022	14.76	0.16	15.154	2.90	0.07
3.143	14.05	0.15	15.275	2.69	0.07
3.271	13.66	0.14	15.403	2.77	0.07
3.399	13.38	0.14	15.531	2.81	0.07
3.527	12.64	0.08	15.658	2.70	0.07
3.655	11.94	0.09	15.787	2.69	0.07
3.783	11.56	0.10	15.915	2.51	0.07

Table B.3. continued.

ν (GHz)	S_ν (mJy)	σ_{S_ν} (mJy)	ν (GHz)	S_ν (mJy)	σ_{S_ν} (mJy)
3.947	*flagged*		16.043	2.77	0.08
4.522	9.44	0.13	16.171	2.57	0.07
4.643	9.70	0.06	16.299	2.51	0.07
4.771	9.58	0.08	16.427	2.53	0.07
4.899	8.99	0.08	16.548	2.74	0.07
5.027	9.04	0.08	16.690	2.64	0.07
5.155	8.82	0.08	16.810	2.48	0.08
5.283	8.46	0.09	16.939	2.48	0.08
5.411	8.28	0.08	17.067	2.48	0.08
5.522	7.94	0.10	17.195	2.50	0.08
5.643	7.97	0.08	17.323	2.32	0.08
5.773	*flagged*		17.451	2.37	0.09
5.899	7.99	0.08	17.579	2.27	0.08
6.026	7.62	0.09	17.707	2.14	0.08
6.154	*flagged*		17.834	2.16	0.09
6.282	7.04	0.09	17.963	2.22	0.10
6.413	7.47	0.09	18.084	2.17	0.10
8.051	5.64	0.06	18.695	2.13	0.05
8.179	5.80	0.06	19.703	2.06	0.05
8.307	5.57	0.06	20.695	2.01	0.05
8.435	5.44	0.06	21.703	1.69	0.06
8.563	5.37	0.06	22.695	1.68	0.06
8.691	5.18	0.06	23.703	1.58	0.06
8.819	5.06	0.06	24.695	1.52	0.06
8.947	5.03	0.07	25.701	1.19	0.06
9.058	5.08	0.06	30.995	1.05	0.07
9.179	4.93	0.06	32.003	0.90	0.08
9.303	4.93	0.06	32.995	1.02	0.08
9.435	4.88	0.06	34.003	0.96	0.08
9.563	4.83	0.06	34.995	0.93	0.08
9.692	4.81	0.06	36.003	0.77	0.10
9.819	4.81	0.06	36.995	0.89	0.10
9.940	4.40	0.07	38.003	0.69	0.13